JGR

RESEARCH ARTICLE

Key Points:
- Ion species and concentration affects calcite surface energy
- Fluids with pH 5–7.5 do not affect calcite surface energy, provided they are saturated with $CaCO_3$
- $MgCl_2$ and $MgSO_4$ seem to induce healing of cracks in calcite

Correspondence to:
A. S. Bergsaker,
a.s.bergsaker@fys.uio.no

The effect of fluid composition, salinity, and acidity on subcritical crack growth in calcite crystals

Anne Schad Bergsaker[1], Anja Røyne[1], Audrey Ougier-Simonin[2,3,4], Jérôme Aubry[2,3,5], and François Renard[2,3,6]

[1]Department of Physics, University of Oslo, Oslo, Norway, [2]Université Grenoble Alpes, ISTerre, Grenoble, France, [3]CNRS, ISTerre, Grenoble, France, [4]The British Geological Survey, Keyworth, United Kingdom, [5]Ecole Normale Superieure de Lyon, Lyon cedex, France, [6]PGP, Department of Geosciences, University of Oslo, Oslo, Norway

Abstract Chemically activated processes of subcritical cracking in calcite control the time-dependent strength of this mineral, which is a major constituent of the Earth's brittle upper crust. Here experimental data on subcritical crack growth are acquired with a double torsion apparatus to characterize the influence of fluid pH (range 5–7.5) and ionic strength and species (Na_2SO_4, NaCl, $MgSO_4$, and $MgCl_2$) on the propagation of microcracks in calcite single crystals. The effect of different ions on crack healing has also been investigated by decreasing the load on the crack for durations up to 30 min and allowing it to relax and close. All solutions were saturated with $CaCO_3$. The crack velocities reached during the experiments are in the range 10^{-9}–10^{-2} m/s and cover the range of subcritical to close to dynamic rupture propagation velocities. Results show that for calcite saturated solutions, the energy necessary to fracture calcite is independent of pH. As a consequence, the effects of fluid salinity, measured through its ionic strength, or the variation of water activity have stronger effects on subcritical crack propagation in calcite than pH. Consequently, when considering the geological sequestration of CO_2 into carbonate reservoirs, the decrease of pH within the range of 5–7.5 due to CO_2 dissolution into water should not significantly alter the rate of fracturing of calcite. Increase in salinity caused by drying may lead to further reduction in cracking and consequently a decrease in brittle creep. The healing of cracks is found to vary with the specific ions present.

1. Introduction

Long-term circulation of fluids influences the brittle and ductile deformation of the Earth's crust, either through the activation of fluid-controlled deformation mechanisms such as pressure solution creep [*Green*, 1984; *Gratier et al.*, 2013] and subcritical crack growth [e.g., *Atkinson*, 1984; *Brantut et al.*, 2013] or through mineralogical transformations that modify the rheological properties of rocks, leading to mineral segregation [*Gratier et al.*, 2015]. Interactions between fluids and rocks play a key role in the destabilization and damage of rocks under stress, and this interplay is considered as one of the parameters that may trigger earthquake ruptures [*Main and Meredith*, 1991], landslides [*Brideau et al.*, 2009], and volcano deformations [*Heap et al.*, 2011]. Some of these deformations are rapid, e.g., during earthquakes, while others occur more slowly. *Atkinson* [1984] was one of the first to systematically review the studies on slow propagation of ruptures in several geological materials at stresses below the threshold necessary to reach dynamic rupture. Such slow crack propagation, also called subcritical crack growth, is responsible for brittle creep in rocks [*Brantut et al.*, 2013, 2014; *Rutter*, 1976; *Croizé et al.*, 2010]. Understanding the role of subcritical cracking in rock deformation is also relevant for prospecting and exploitation of hydrocarbons [*Fan et al.*, 2012] and geothermal resources [*Ghassemi*, 2012], and for the long-term stability of geological reservoirs where CO_2 could be permanently stored [*Rohmer et al.*, 2014]. Finally, microfractures that develop in rocks through subcritical crack growth modify the elastic, strength, and fluid transport properties of these rocks [*Anders et al.*, 2014].

Griffith [1921] proposed that the fracturing of materials is controlled by the growth of preexisting submicroscopic flaws. According to Griffith's theory, a fracture is able to grow when the mechanical energy released by the system due to fracture propagation, $\mathcal{G}$, is greater than the energy needed to create two new surfaces, 2γ. The system is in mechanical equilibrium when $\mathcal{G}_0 - 2\gamma = 0$ (J/m^2). Later, *Orowan* [1944] discovered experimentally that glass can break at stresses far below their ordinary strength when a moderate stress is applied during an extended period of time. The more general expression of the fracture criterion is
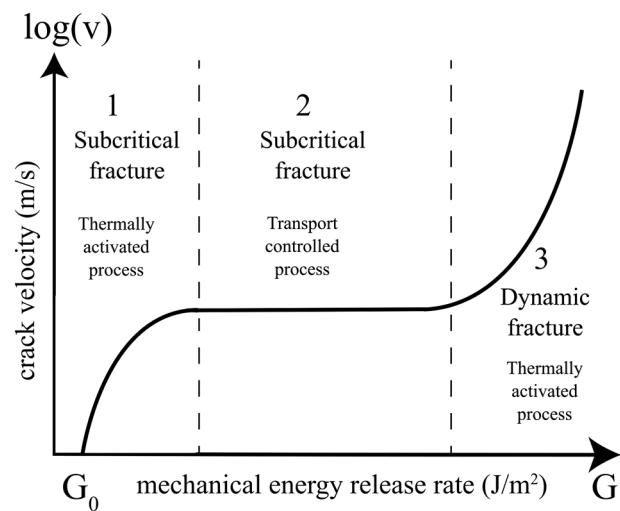
Figure 1. Energy release rate $\mathcal{G}$ as a function of crack velocity (modified from *Rostom et al.* [2013]). Vertical dashed lines show the boundaries between subcritical crack propagation on the left (1) and dynamic fracturing on the right (3), connected by a transport limited regime characterized by a near constant crack velocity (2).

given as $\mathcal{G}_0 - 2\gamma_e = 0$, where the subscript e refers to the chemical environment in contact with the fracture surfaces. The phenomenon of altering the mechanical strength of a solid by introducing adsorption-active media into the system is known as the Rehbinder effect [*Shchukin et al.*, 2006]. As this effect is only dependent on the initial surface energy of the solid and the ions introduced into the system, similar results ought to be expected for calcitic rocks and pure calcite. Other mechanisms that may contribute to subcritical cracking include weakening reactions at the crack tip, e.g., *Charles* [1958]; preferential dissolution at the crack tip with rapid removal of dissolved species [*Atkinson*, 1984]; or even environmentally controlled microplasticity with pileup of dislocations in the process zone around the crack tip [*Atkinson*, 1984].

Subcritical fracture propagation is typically found to display three different regimes [*Atkinson*, 1984; *Wan et al.*, 1990] (see Figure 1), of which regimes 1 and 2 are the domains of interest in the present study. Stress-dependent kinetic processes give a strongly load dependent crack velocity in regime 1. In regime 2, the transport of reactive species to the crack tip is the rate limiting process; hence, the fracture velocity will only be weakly dependent on load. The lower limit for fracture propagation, $\mathcal{G}_0$, is not directly measurable in experiments [*Wan et al.*, 1990]. Therefore, the fast decrease of crack velocity when $\mathcal{G}$ decreases toward a limit value is used as a weak experimental definition of the upper limit of the threshold $\mathcal{G}_0$ in crack growth experiments [*Lawn*, 1993]. Around this region, the crack velocity can typically be expressed as a hyperbolic sine function of $\mathcal{G}$ [*Wan et al.*, 1990], corresponding to a thermal activation barrier that decreases linearly with $\mathcal{G}$. The relationship between the energy release rate $\mathcal{G}$ and the crack tip velocity v is then

$$v = 2\frac{kT}{h}a_0 \exp\left(\frac{-\Delta F}{kT}\right)\sinh\left(\alpha\frac{\mathcal{G}-\mathcal{G}_0}{kT}\right), \tag{1}$$

where k and h are Boltzmann's and Planck's constants, respectively, T is the absolute temperature, a_0 is a characteristic atomic spacing, α is an activation area, and ΔF is the height of the quiescent energy barrier. These last two parameters are determined by the intrinsic bond rupture energy [*Wan et al.*, 1990].

Theoretically, healing of small fractures is possible through a thermally activated process, just like fracture growth [*Brantley et al.*, 1990; *Stavrinidis and Holloway*, 1983; *Lawn*, 1993]. It is only a matter of achieving small enough apertures to allow for bonds to reform. There is, however, expected to be a certain hysteresis in such a setup; the healed crack will not be as strong as the *virgin* crack, due to incomplete removal of adsorbed species and lattice mismatch between the fracture surfaces. According to *Lawn* [1993], the level of hysteresis is governed by the chemistry of the system. Dependence on time and heat has been studied for quartz [*Brantley et al.*, 1990] and glass [*Stavrinidis and Holloway*, 1983]. The dependence on specific ions in the fluid remains to be studied.

Table 1. List of Experiments, Experimental Conditions, and Values of $\mathcal{G}_0$ Obtained

Experiment	Fluid	Vertical Point Load at the Onset of Relaxation (N)	Recorded Duration of Relaxation (s)	$\mathcal{G}_0$ (J/m^2)	pH Initial	pH Final	Ionic Strength (mol/l)
20150512_CA13	Air humidity	2.8	1,800	0.45	-	-	-
20150513_CA14	Air humidity	2.42	562	0.32	-	-	-
20150515_CA15	Air humidity	2.1	6,350	0.30	-	-	-
20150518_CA16	Air humidity	2.8	149	0.45	-	-	-
20150519_CA17	Air humidity	2.68	640	0.39	-	-	-
20150520_CA18	Distilled water	2.7	47	0.32	5.5	-	-
20150528_CA21	Distilled water	2.35	2,700	0.35	5.5	-	-
20150608_CA26	Acetic acid, saturated with CaCO$_3$ (pH = 7)	2.3	1,250	0.31	7.1	7.1	1.8
20150609_CA27	Acetic acid, saturated with CaCO$_3$ (pH = 7)	2.38	7,400	0.35	7.0	7.0	1.8
20150611_CA28	Acetic acid, saturated with CaCO$_3$ (pH = 5.5)	2.5	9,500	0.34	5.5	5.5	1.4
20150615_CA29	Acetic acid, saturated with CaCO$_3$ (pH = 6)	2.3	11,800	0.29	6.1	6.0	1.6
20150616_CA30	Acetic acid, saturated with CaCO$_3$ (pH = 6)	1.95	13,000	0.31	5.9	6.0	1.6
20150625_CA31	Distilled water	2.35	15,800	0.30	5.5	-	-
20150630_CA32	Acetic acid, saturated with CaCO$_3$ (pH = 7.5)	2.35	11,000	0.30	7.5	7.5	1.6
20150706_CA33	Acetic acid, saturated with CaCO$_3$ (pH = 5.5)	2.15	18,000	0.27	5.6	5.7	1.4
20150707_CA34	Acetic acid, saturated with CaCO$_3$ (pH = 7.5)	2.2	16,500	0.26	7.5	7.5	1.6
20150708_CA35	Acetic acid, saturated with CaCO$_3$ (pH = 6)	2.32	15,800	0.36	6.0	6.1	1.6
20150709_CA36	Acetic acid, saturated with CaCO$_3$ (pH = 7)	2.5	16,000	0.33	7.0	7.0	1.8
20150716_CA37	Acetic acid, saturated with CaCO$_3$ (pH = 7.5)	2.5	14,000	0.27	7.5	7.5	1.6

Calcite is a major constituent of the Earth's crust, and it is the primary constituent in limestones, including chalk, which has gained interest lately due to its potential as a storage reservoir rock for captured CO_2 [*Emberley et al.*, 2005]. It has been shown that the mechanical strength of chalk is significantly affected by both water activity [*Risnes et al.*, 2005], and the presence of salts such as NaCl, Na_2SO_4, or $MgCl_2$ [*Megawati et al.*, 2012; *Madland et al.*, 2011; *Zangiabadi et al.*, 2011]. *Heggheim et al.* [2005] found that the water weakening effect seen in chalk must be at least partly chemical in nature. This is supported by *Gutierrez et al.* [2000], as well as *Baud et al.* [2009], who demonstrated a water weakening effect in Majella grainstone and Saint-Maximin limestone. It has also been found that synthetic sea water and water with moderately high concentrations of $MgCl_2$ (0.1–0.2 *M*) cause increased strain rates in stressed chalk when comparing with pure water and water with NaCl [*Madland et al.*, 2011]. Several studies have also found that the concentration of Na_2SO_4 affects the strength of chalk, with reduced strength for higher concentrations [*Korsnes et al.*, 2014; *Heggheim et al.*, 2005].

To our knowledge, only *Henry et al.* [1977] have shown a nontrivial dependency of crack growth on pH in calcitic rocks. A number of studies linking pH to crack growth have, however, been done on quartz [*Atkinson and Meredith*, 1981] and glass [*Wiederhorn and Johnson*, 1972].

Table 2. List of Experiments, Experimental conditions, and Values of $\mathcal{G}_0$ Obtained[a]

Experiment	Fluid	Vertical Point Load at the Onset of Relaxation (N)	Duration of Fracture Closing (s)	$\mathcal{G}_0$ (J/m^2)	Ionic Strength (mol/l)
140724	Distilled water with 0.3 M MgSO$_4$	2.47	1320	0.31	1.2
140725	Distilled water with 0.4 M MgCl$_2$	2.64	250	0.35	1.2
140910	Distilled water with 0.004 M Na$_2$SO$_4$	2.57	-	0.40	0.012
140925	Distilled water with 0.003 M MgSO$_4$	2.25	3200	0.31	0.012
141016	Distilled water with 0.012 M NaCl	2.34	-	0.28	0.012
141017	Distilled water with 0.004 M MgCl$_2$	2.34	1990	0.26	0.012
141024	Distilled water with 0.4 M Na$_2$SO$_4$	2.43	1240	0.30	1.2
141104	Distilled water with 0.4 M MgCl$_2$	2.45	2260	0.33	1.2
141118	Distilled water with 1.2 M NaCl	2.64	-	0.32	1.2
141121	Distilled water with 0.004 M Na$_2$SO$_4$	2.50	-	0.34	0.012
141210	Distilled water with 0.3 M MgSO$_4$	2.81	-	0.35	1.2
150113	Distilled water with 0.004 M MgCl$_2$	2.58	-	0.32	0.012
150114	Distilled water with 0.003 M MgSO$_4$	2.70	1540	0.34	0.012
150115	Distilled water with 0.4 M Na$_2$SO$_4$	2.55	-	0.29	1.2
150119	Distilled water with 0.4 M MgCl$_2$	2.51	1240	0.34	1.2
150123	Distilled water with 0.003 M MgSO$_4$	2.52	3130	0.28	0.012
150126	Distilled water with 0.004 M MgCl$_2$	2.56	1940	0.32	0.012
150310	Distilled water with 0.4 M Na$_2$SO$_4$	2.48	10, 10, 1450, 1520	0.25	1.2
150313	Distilled water with 0.4 M MgCl$_2$	2.37	20, 10, 2160, 1440	0.27	1.2
150318	Distilled water with 0.3 M MgSO$_4$	2.58	11, 10, 1640, 1550	0.37	1.2
150420	Distilled water with 0.004 M MgCl$_2$	2.72	10, 7, 1270, 1150	0.36	0.012
150511	Distilled water with 0.003 M MgSO$_4$	2.44	7, 300, 610, 950, 1210, 1830, 300	0.26	0.012
150513	Distilled water with 0.4 M Na$_2$SO$_4$	2.47	0, 10, 30, 60, 300, 620, 1930, 30	0.26	1.2
150518	Distilled water with 0.4 M Na$_2$SO$_4$	2.33	0, 11, 30, 60, 300, 1200, 30	0.26	1.2
150526	Distilled water with 0.004 M Na$_2$SO$_4$	2.48	0, 20, 40, 60, 300, 1210, 40	0.32	0.012

[a]All solutions were saturated with CaCO$_3$.

In the present study we expand the testing conditions of *Røyne et al.* [2011] and *Rostom et al.* [2013] to investigate the effect of (1) the fluid pH and (2) the fluid composition and salinity on the crack propagation and healing of cracks in calcite single crystals.

2. Materials and Methods

Two sets of experiments were performed in this study. In the first set, the effect of pH on fracture propagation was addressed, while in the second set the salt type and concentration was varied and healing of fractures was also studied. A newly built double torsion experimental setup at the Université Grenoble Alpes was used for the first set of experiments. For the second set, we used the same double torsion rig as in *Rostom et al.* [2013], built at the University of Oslo. A few experiments were conducted at the same experimental conditions using both rigs and found to yield the same results. In total, 44 successful experiments were performed, and the conditions are given in Tables 1 and 2.

### 2.1. Double Torsion Apparatus and Experimental Conditions

The concept of double torsion testing was developed by *Evans* [1972]. It involves a flat sample with an initial crack, loaded between three points (see Figure 2d). When the load is increased, the sample is bent, resulting in a mode I crack propagation along the centre of the sample. In a typical stress relaxation experiment, the indenter is stopped at a fixed position, and the load relaxes as the sample compliance increases due to the fracture propagation. An advantage of the double torsion method is that the energy release rate can be calculated from the measured load, independent of crack length for the middle part of the sample [*Shyam and Lara-Curzio*, 2006].
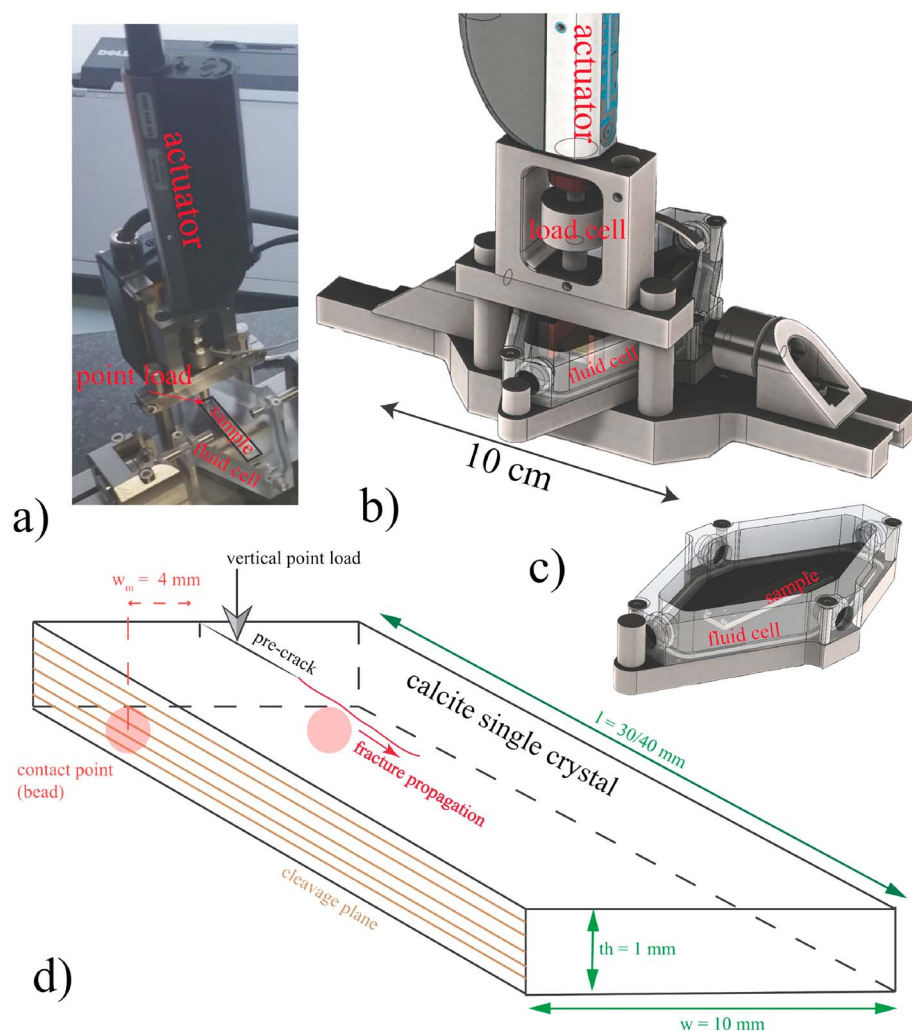
Figure 2. (a) Picture of double torsion apparatus built at Université Grenoble Alpes, with the sample in the fluid cell and the point load applied by the actuator. (b) Sketch of the double torsion apparatus showing the actuator and the load cell. (c) The sample is located in the Plexiglas fluid cell. (d) Schematic view of the calcite single-crystal sample, the initial notch (precrack), and the vertical load applied exactly in the middle distance of the two contact points (red beads). The calcite was cut with cleavage direction parallel to the direction of fracture propagation.

Calcite monocrystals were provided by the company Crystan Ltd., with dimensions of $10 \times 40 \times 1$ mm (for the experiments with varying pH), and $10 \times 30 \times 1$ mm (for the experiments testing the effect of ion species). The crystals were cut so that the $40/30 \times 1$ mm side was parallel to the $10\bar{1}4$ cleavage plane (see Figure 2d), and the largest surfaces were polished to optical quality. Cutting the crystals in such a way ensures that the fracture will propagate through the sample parallel to the cleavage plane. Prior to mounting, each sample was scratched with a caliper to create a $3-10$ mm long initial crack parallel to the cleavage plane (Figure 2d) and then placed in a fluid cell in the double torsion apparatus. The experimental setup was located in a temperature controlled room to reduce thermal noise. All experiments were performed at room temperature, close to $23 \pm 1.5°C$ and under atmospheric pressure and humidity conditions. Fracture propagation was monitored optically, through time-lapse photography. Note that the imaged crack is a reflection of white light inside the crack. This means that in order for the crack to be visible, it must have an aperture of the same order of magnitude as the wavelength of visible light; hence, the measured crack tip position will always be located slightly behind the actual crack tip position (see Figure 3).

In some experiments imperfect alignment of the sample and indenter caused the fracture to curve away from the midplane of the sample. These experiments were discarded.
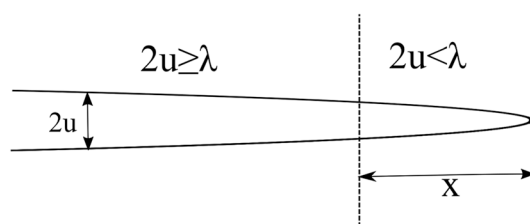
Figure 3. Simple sketch showing the difference between the measured crack length and the actual crack length, where $2u$ is the crack aperture and λ is the wavelength of white light. x is the difference between measured crack length and actual crack length.

2.1.1. Grenoble Double Torsion Apparatus Description and Loading Protocol

The setup used in Grenoble for the first set of experiments is shown in Figure 2. The load is applied with the tip of a linear piezo actuator (Newport, LTA-HL). Once the tip is in contact with the sample, a vertical displacement of the actuator in the range 0.015–0.016 mm is applied at a velocity of 0.005 mm/s. This induces an increase of the load to a value between 2.5 and 3 N, which is large enough to promote propagation of the initial notch crack but also low enough to avoid a dynamic fracture propagation across the whole sample. The crack starts propagating at a velocity close 10^{-2} m/s and then slows down to velocities around 10^{-8} m/s, or in some cases 10^{-9} m/s, as relaxation proceeds. Pictures of the fracture propagation were taken at a rate of 1 to 10 images per second with a camera (Prosilica GC2450, pixel size 3.45 μm × 3.45 μm). A light-emitting diode cold light (Amaran 528W) was used as a light source. The load is continuously monitored using a force gauge recorded at a frequency of 100 Hz. The duration of the experiments was varied from minutes, to probe the largest velocities and large values of $\mathcal{G}$, up to 3 h to probe the lowest velocities.

The device also includes a laser displacement meter (Keyence LK-G10) with a wavelength of 655 nm that measures the vertical deformation of the actuator sample holder column during sample loading. The vertical displacement was found to be less than 1 μm, whereas the flexure of the calcite sample is at least 10 times larger. Therefore, most of the elastic strain energy is stored into the sample during loading and the apparatus is considered as infinitely stiff compared to the sample.

2.1.2. Oslo Double Torsion Apparatus Description and Loading Protocol

The exact setup used is shown in *Rostom et al.* [2013]. Here we will only provide a brief summary. As in the Grenoble double torsion apparatus, the sample is loaded using a linear piezo actuator (PI, N-381). This particular actuator can move as slowly as 10^{-4} m/s, which is the velocity used during most of the experiment. The load is increased until it reaches a maximum where load relaxation due to fracture propagation becomes greater than the load increase due to the indenter displacement. Fracture velocities never exceed 10^{-3} m/s in this setup. At this maximum the actuator is stopped and kept stationary while the crack propagates. Prior to the loading and relaxation cycle, the initial crack is made to propagate so that each experiment is started from the same fracture length. This also ensures that crack propagation during loading and relaxation starts from a smooth, sharp, and straight crack. After loading, the sample is allowed to relax for around 2 h. At this point the load would have stabilized significantly, and the fracture propagation velocity reduced by 3–4 orders of magnitude.

The position of the actuator (internal sensor with 20 nm resolution), the load recorded by the load cell (Omega LC703-10), and the temperature in the room (measured using thermistors) were all recorded at a frequency of 20 Hz, using a LabVIEW acquisition program. The load cell has a maximum range of 44 N and a resolution of 10^{-3} N including noise and effects of minor temperature fluctuations. The fracture length was monitored optically, using a camera (Prosilica GC2450), taking time-lapse images, with a maximum frequency of 4 Hz. The resolution was around 13.7 μm.

After measuring the initial subcritical fracture propagation, the load was reduced to ∼0.59 ± 10% N and kept constant at a relaxation time period varying from zero to about 20–30 min. Subsequently, the load was increased again until it reached the level it had been at the end of the initial fracture propagation. In some experiments, this cycle was repeated for relaxation hold times of 0, 10, 30, 60, 300, 600, and 1200 s, and finally 30 s again, to check for history dependence. We tested for several different time intervals in order to see if the level of fracture closing was dependent on the time it was allowed to close. Similarly, we also ran a few tests in which the speed of the actuator during load reduction was varied by an order of magnitude;

i.e., both a velocity of 10^{-4} m/s and 10^{-3} m/s was tried in order to see if the velocity of the actuator affected the closing of the crack.

At the end of each experiment, the sample was reloaded until the sample broke in two. The topography of the entire fracture surface was measured using a white light interferometer (Wyko NT1100 from Veeco), which has a height resolution close to 1 nm. Seven of the samples were imaged at high resolution using a scanning electron microscope (Hitachi SU5000 FE-SEM). Especially the area where potential healing had taken place was studied in detail. The purpose of this was both to see if there were variations within one surface, as well as between different samples.

2.2. Varying PH: Solutions Used

Nineteen successful experiments (Table 1) were performed with three types of fluids: air (i.e., no fluid was added to the fluid cell), distilled water in equilibrium with atmospheric CO_2 (measured pH 5.5), and acidic aqueous fluids buffered with calcium carbonate. Acetic acid provided by Roth© was used to prepare a stock solution of pH 4 at 0.97 M, which was then diluted to reach higher pH. Calcium carbonate powder provided by Chem-Lab was added to the stock solution to obtain solutions saturated with calcite with pH in the range 5.5 – 7.5. The pH of the solutions was measured before and after most of the experiments using a calibrated laboratory pH meter, and the calcium concentration of relevant solutions was analyzed using induced coupled plasma-atomic emission spectroscopy. In all experiments with acetic acid where the pH was measured before and after, the pH variation during experiments was negligible (see Table 1) and we therefore consider that fluid pH remained constant during the experiments. After some experiments, the cracked sample was observed from above using an optical microscope or a scanning electron microscope.

The ionic strength I of the solutions is calculated using the relation $I = 0.5 \times \Sigma c_i z_i^2$ where c_i is the concentration of charged species in the solution and z_i is the number of positive or negative charges of each ion: CH_3CO^{2-}, H_3O^+, OH^-, Ca^{2+}, HCO_3^-, and CO_3^{2-}. The concentrations of Ca^{2+} and the pH are measured directly, and the other concentrations are calculated from the dissociation constant of acetic acid at 25°C (pKa = −4.8) and the dissociation constants of carbonic acid given in a 1 M ionic strength solution at 25°C (pKa1 = −5.94, pKa2 = −9.54), as given in the Table 2 of *He and Morse* [1993]. The pH and ionic strength are given in the Table 1.

When an acidic fluid with a pH lower than 5 was used, bubbles formed on the calcite surfaces. As these could lift or even move the sample within the fluid cell, the measured force cannot be used to calculate the energy release rate accurately. These experiments were therefore discarded from the present study.

2.3. Varying Salts and Salinity: Solutions Used

Eight different electrolyte solutions with two different ionic strengths, referred to as high (1.2 M, H) and low (0.012 M, L) were used (see Table 2). All solutions were saturated with $CaCO_3$. In total, 25 successful experiments were conducted. Fewer experiments were performed with NaCl than with the other solutions, as we were able to use data from *Rostom et al.* [2013] for this solution. The pH of the different solutions was not measured. However, using PHREEQC [*Parkhurst et al.*, 1999], we can simulate solutions used in this study. Assuming the water is equilibrated with the CO_2 in the atmosphere, and saturated with calcite, we find that the pH of the different solutions are all within 8.24 – 8.50. No clear correlation between the pH of the solutions and the measured results was seen.

2.4. Data Processing

First, the vertical position of the loading actuator tip and the corresponding vertical applied force are plotted in order to select the period of crack relaxation during the experiment (Figure 4a). Second, the pictures from the beginning to the final time of fracture propagation were identified and selected. The initial image was used as a reference background and subtracted from each of the following images. A threshold was chosen to determine the exact position of the crack tip.

Using these data, the crack tip position x at each time t can be extracted and its instantaneous velocity is calculated as $v = dx/dt$ by fitting a straight line to a suitable number of data points.

The sample is characterized by its compliance, C, given as

$$C \approx \frac{\Delta}{P} \approx \frac{3S_m^2 a}{St^3 G \psi(\tau)},\qquad(2)$$
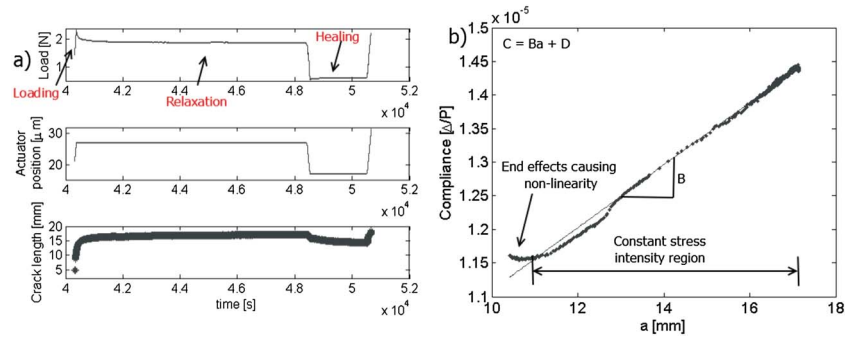
Figure 4. (a) Plots of the vertical load (top), vertical displacement of the actuator tip (middle), and measured crack length (bottom). Loading, relaxation, and healing are indicated with arrows. (b) Calculated compliance for sample 141017 (see Table 2) plotted against crack length. The curve is mostly linear, with deviation from a straight line in the beginning, due to end effects.

where P is the load, Δ is the deformation of the sample, which in our case was given by the change in actuator position, S_m is half the distance between the supports, S and t are the sample width and thickness respectively (see Figure 2d), G is the shear modulus for calcite ($G = 32.8$ GPa *Chen et al.* [2001]), ψ is a geometric correction factor given as $\psi = 1 - 0.6302\tau + 1.20\tau \exp(-\pi/\tau)$ where $\tau = 2t/S$, and a is the crack length [*Shyam and Lara-Curzio*, 2006]. It has been found in several setups that the compliance relates to crack length such that

$$C = \frac{\Delta}{P} = Ba + D, \tag{3}$$

which includes the stiffness of the rig, D. Given this linear relationship (see Figure 4b), the fracture velocity can be expressed as

$$v = \frac{1}{BP}\left(\frac{d\Delta}{dt} - \frac{\Delta}{P}\right)\frac{dP}{dt}, \tag{4}$$

where B is found by linear fitting according to equation (3). In the case where Δ is constant, this can be further simplified to

$$v = \frac{-\Delta}{BP^2}\frac{dP}{dt}, \tag{5}$$

or alternatively (if D is large enough not to be neglected)

$$v = -\frac{P_i}{P^2}\left(a_i + \frac{D}{B}\right)\frac{dP}{dt}, \tag{6}$$

where subscript i is some instantaneous value. As a check, the velocities given by equations (4) and (6) were calculated and compared to the velocity based on the derivative of the crack length and found to agree.

Assuming the crack front does not change with crack propagation, the energy release rate can then be expressed as

$$\mathcal{G} = \frac{P^2}{2t}\left(\frac{dC}{da}\right) = \frac{3P^2 S_m^2}{2St^4 G\psi}. \tag{7}$$

The expression for the energy release rate is thus independent of crack length in this setup, as long as the fracture tip is far enough from the edges of the sample to avoid edge effects [*Shyam and Lara-Curzio*, 2006]. The main sources of uncertainty in $\mathcal{G}$ are the thickness of the sample t (2%), the shear modulus G (5–10%), and the position of the supports relative to the middle of the sample S_m (5%), giving a total absolute uncertainty of about 13%. In our experiments the shear modulus of all samples were the same as they were produced from the same initial calcite crystal, the main uncertainty being in the sample thickness, and the initial position of the sample.

The crack tip position as a function of time and the relaxation of the force and the energy release rate $\mathcal{G}$ as a function of crack velocity v for one experiment are shown in Figure 5.
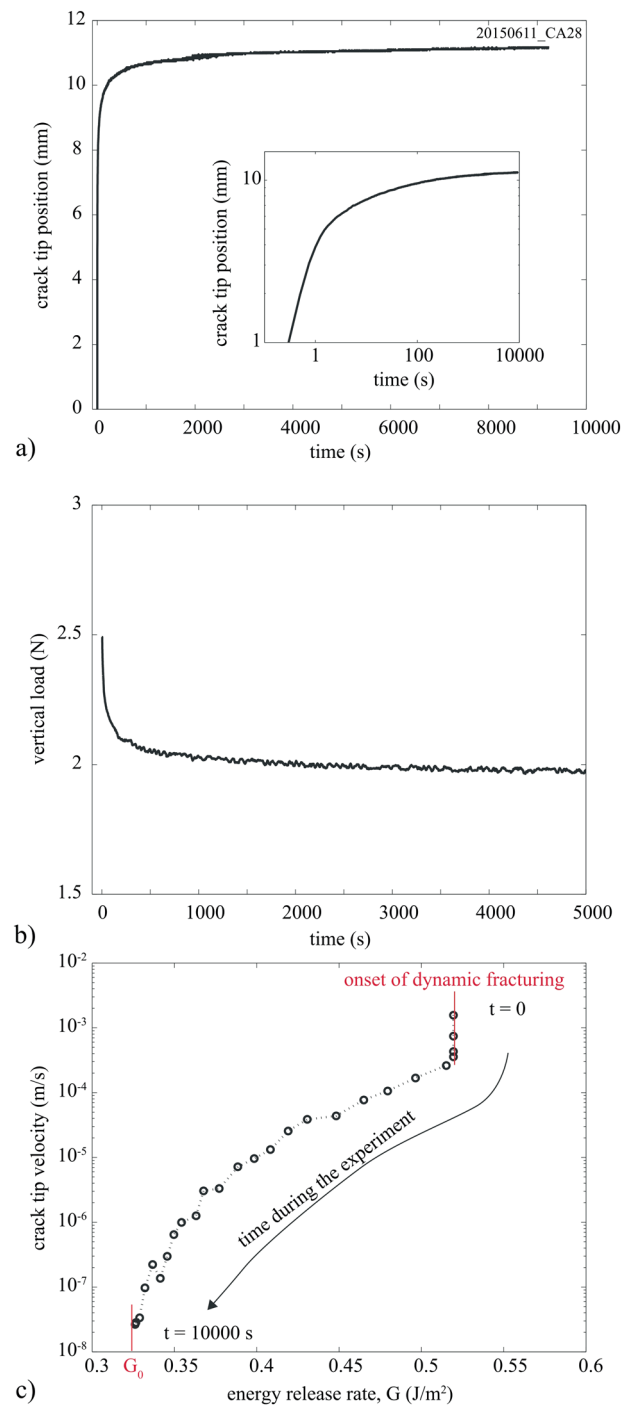
Figure 5. Data processing for experiment 20150611_CA28 (see Table 1). (a) Position of the crack tip as a function of time. The inset shows the same evolution with log-log axis. (b) Vertical load as a function of time showing the relaxation. (c) Relationship between the strain energy released and the crack tip velocity. The lowest energy rate $\mathcal{G}_0$ corresponds to the onset of subcritical crack propagation.

To estimate the value of $\mathcal{G}_0$, the experimental curve $\mathcal{G}$ versus v (Figures 6–8) was fitted for each experiment using the hyperbolic sinus function (equation (1)) using the following parameters: $T = 298$ K, $k = 1.38 \times 10^{-23}$ m^2 kg s^{-2} K^{-1}, $h = 6.63 \times 10^{-34}$ m^2 kg s^{-1}, $\Delta F = 9.1 \times 10^{-20}$ J, $a_0 = 5 \times 10^{-10}$ m, which corresponds to the atomic cell size of calcite [*Stipp and Hochella Jr*, 1991], and $\alpha = 1.4 \times 10^{-19}$ m^2. All these parameters were set constant for calcite, and the value of $\mathcal{G}_0$ was then calculated by a least squares method.
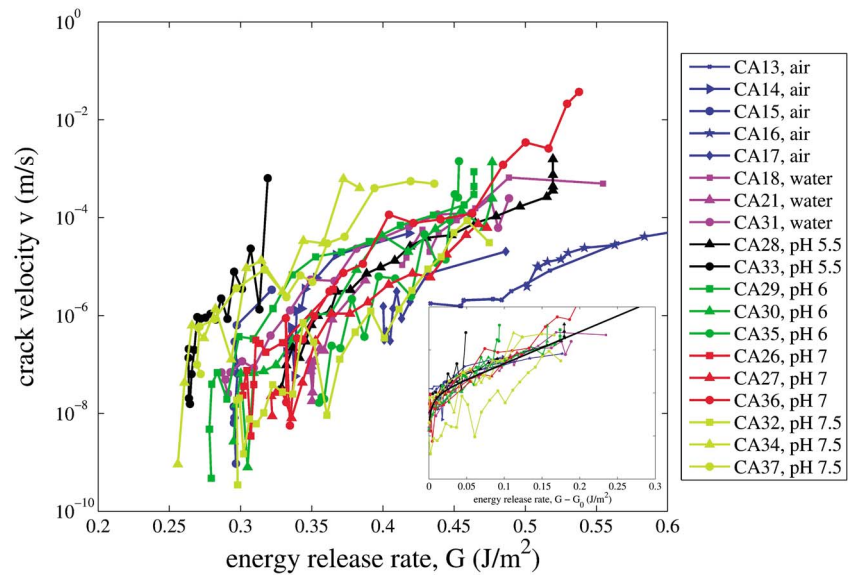
Figure 6. Crack velocities as a function of the energy release rate $\mathcal{G}$ all experiments with varying fluid pH (Table 1). The inset shows the data collapse of the velocity versus $(\mathcal{G} - \mathcal{G}_0)$ and the bold line corresponds to the fit using equation (1).

### 2.5. Limitations of the Experimental Procedure and Reproducibility of the Results

Several caveats related to the double torsion experiments should be discussed. First, when the calcite sample is notched with the caliper, a precrack is formed. However, subsequent and potentially erratic propagation of the precrack may occur. In particular, uncontrolled propagation could happen following the insertion of the sample into the fluid-filled cell.

Furthermore, the precrack tends to be significantly rougher than the perfectly linear crack propagating from it. These uncontrolled characteristics of the precrack are expected to cause some variability in the initial load required to trigger propagation of the crack. In order to address this issue the precrack was deliberately propagated a small distance into the sample, as part of the experimental procedure used with the Oslo setup. However, this precaution should only affect the load needed to start propagating the crack, leaving $\mathcal{G}_0$
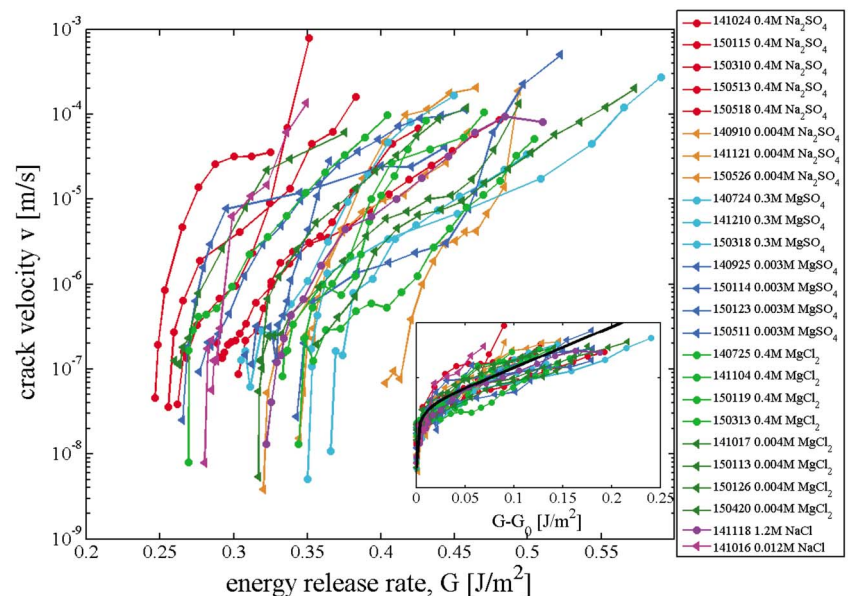
Figure 7. Energy release rate, $\mathcal{G}$, plotted against crack velocity for all experiments. The inset shows the data collapsing when $\mathcal{G}_0$ is subtracted. The thick black line represents the fitted function using equation (1).
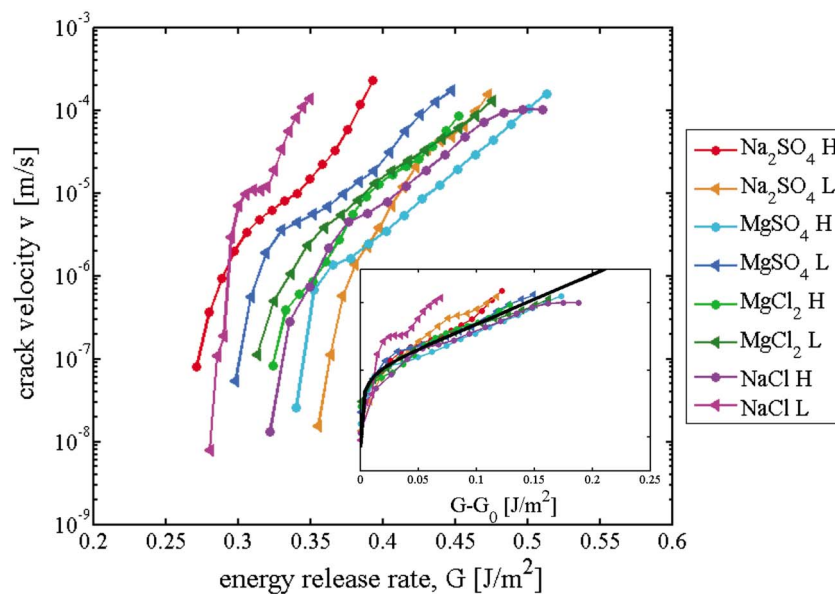
Figure 8. Energy release rate, $\mathcal{G}$, plotted against crack velocity, v, averaged across experiments with same salts and ionic strength (H = high, L = low). The inset shows the corresponding data collapse, with the same fitted line as shown in Figure 7.

essentially unchanged, unless frictional resistance occurs between the two sections of the calcite crystal, owing to an overly large roughness of the precrack.

Second, if the tip of the linear actuator is not perfectly centered on the sample, the crack may not propagate linearly in pure mode I but may include mode III segments. As a consequence, the double torsion technique requires a nearly perfect positioning of the sample to ensure good reproducibility. The issue of centering the precracked sample relative to the actuator is believed to be the greatest source of variability in our results.

3. Results

In all successful experiments the cracks propagated linearly, along the center of the sample, until the experiments were stopped. Microscope observations (Figure 9) show that there is some damage in the crystal near the initial notch made with a caliper. However, after the initial notch the trace of the crack is linear, within the resolution of both the optical microscope and the scanning electron microscope.

Experimental results are summarized in Tables 1–3.
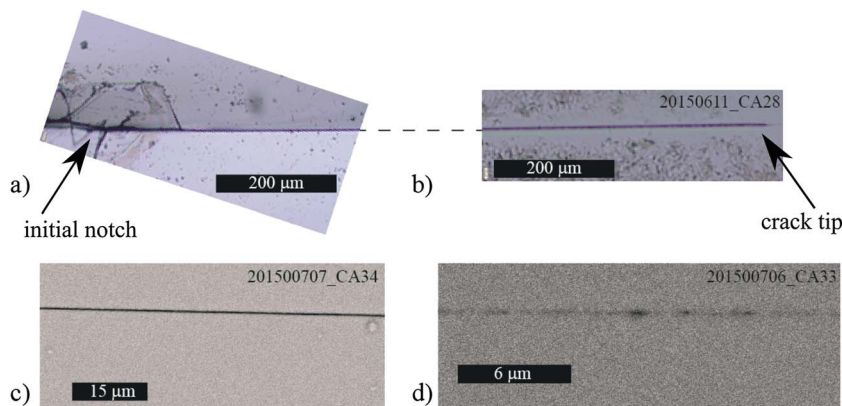
Figure 9. (a and b) Optical and (c and d) scanning electron microscope images of the crack at different scales showing almost linear propagation along a calcite cleavage. Some damage near the initial notch (Figure 9a) is seen as secondary fractures which, for this experiment, did not induce perturbation of the linear propagation of the crack (Figure 9b). Near the tip, the crack becomes thinner and thinner (Figure 9c) until the lowest resolution of 50 nm of the images is reached.

Table 3. Summary of Data Presented in Tables 1 and 2[a]

| Fluid	Velocity Interval (m/s)	$\mathcal{G}_0$ Interval (J/m^2)	Average $\mathcal{G}_0$
Air	$10^{-9} - 10^{-4}$	$0.30 - 0.45$	0.38
Distilled water	$10^{-8} - 10^{-2}$	$0.30 - 0.35$	0.32
Acetic acid, pH = 5.5	$10^{-8} - 10^{-2}$	$0.27 - 0.34$	0.30
Acetic acid, pH = 6.0	$10^{-9} - 10^{-2}$	$0.29 - 0.36$	0.32
Acetic acid, pH = 7.0	$10^{-8} - 10^{-5}$	$0.31 - 0.35$	0.33
Acetic acid, pH = 7.5	$10^{-9} - 10^{-5}$	$0.26 - 0.30$	0.28
1.2 M NaCl	$10^{-8} - 10^{-4}$	0.32	0.32
0.012 M NaCl	$10^{-8} - 10^{-4}$	0.28	0.28
0.3 M MgSO$_4$	$10^{-8} - 10^{-3}$	$0.27 - 0.35$	0.34
0.003 M MgSO$_4$	$10^{-8} - 10^{-3}$	$0.26 - 0.34$	0.30
0.4 M MgCl$_2$	$10^{-8} - 10^{-4}$	$0.27 - 0.35$	0.32
0.004 M MgCl$_2$	$10^{-8} - 10^{-4}$	$0.26 - 0.36$	0.31
0.4 M Na$_2$SO$_4$	$10^{-8} - 10^{-4}$	$0.25 - 0.30$	0.27
0.004 M Na$_2$SO$_4$	$10^{-8} - 10^{-4}$	$0.32 - 0.40$	0.36

[a]All fluids except air and distilled water are saturated with CaCO$_3$.

3.1. Subcritical Crack Growth in Air and Distilled Water

Several experiments were performed on the Grenoble double torsion setup in atmospheric humidity and in distilled water. With distilled water, $\mathcal{G}_0$ varies between 0.30 and 0.35 J/m^2, with an average of 0.32 J/m^2, very close to the value of 0.30 J/m^2 measured by *Røyne et al.* [2011]. For atmospheric humidity experiments, values lie in the range 0.30–0.45 J/m^2, with an average of 0.38 J/m^2, which is consistent with the formation of a capillary condensate at the crack tip [*Grimaldi et al.*, 2008]. The presence of water in the crack would make the surface energy of calcite during fracture propagation identical to that in submerged conditions, but capillary forces acting against the opening of the fracture make the observed threshold for fracture propagation higher [*Wan and Lawn*, 1990]. The energy released during crack propagation in the presence of liquid water is smaller than with atmospheric humidity on average, as previously reported for both calcite and rocks [*Atkinson*, 1984].

3.2. Effect of pH

In the experiments with variable pH, made with the Grenoble double torsion setup, crack velocities were measured in the range $10^{-8} - 10^{-2}$ m/s (see Table 3). The $\mathcal{G}$-v curves (Figure 6) display mostly regime 1 behavior
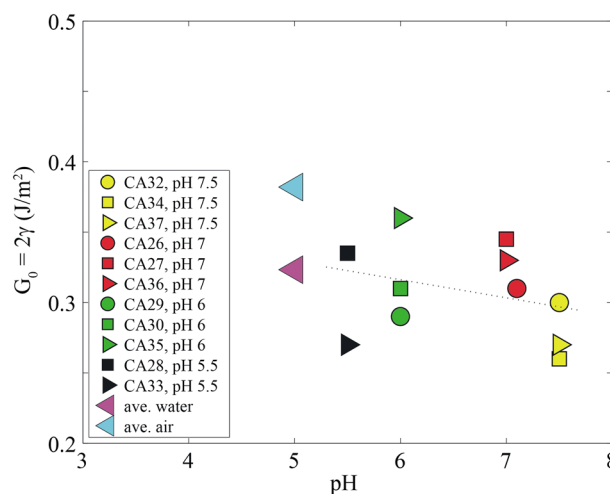
Figure 10. Influence of pH on the value of the energy release rate $\mathcal{G}_0$ at the onset of crack propagation. Overall, the variation of pH does not change $\mathcal{G}_0$ significantly. The dashed line represents a linear fit of the data. The average values of $\mathcal{G}_0$ for distilled water in equilibrium with the atmosphere and for atmospheric humidity (air) are also given.
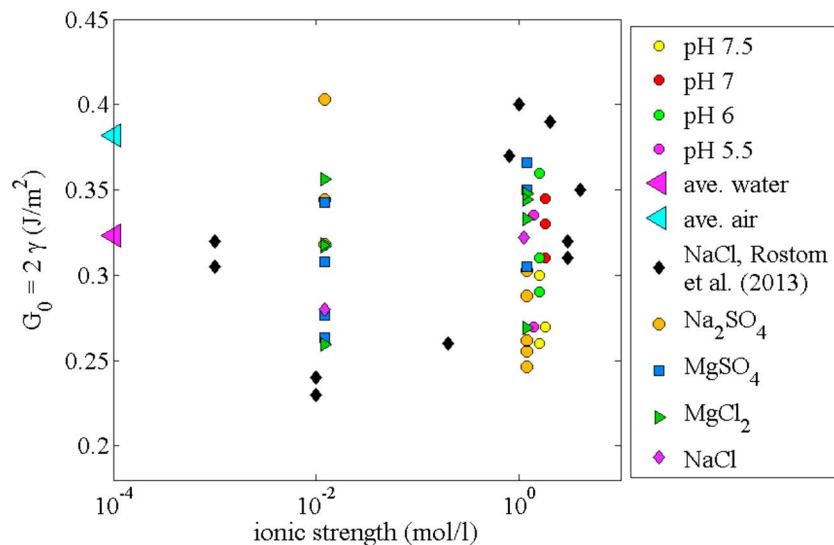
Figure 11. Effect of ionic strength on the energy release rate $\mathcal{G}_0$ at the onset of crack propagation. Black diamonds are data of *Rostom et al.* [2013], where ionic strength was controlled with NaCl solutions. The average values of $\mathcal{G}_0$ for distilled water in equilibrium with the atmosphere and for atmospheric humidity (air) are also given.

and can be collapsed onto a single curve using equation (1). In some experiments, (see, for instance, CA28, Figure 6) the crack starts propagating close to dynamic fracturing (regime 3 fracture propagation).

For each experiment, the value of the energy release rate $\mathcal{G}_0 = 2\gamma$, where γ (J/m^2) is the interfacial energy of calcite, can be estimated for the various values of pH (Figure 10). When applying a linear regression to all data, a positive trend can be detected that could be interpreted as corresponding to a slight influence of pH on subcritical crack propagation. However, when considering the experimental variability, the hypothesis of a null influence of pH cannot be ruled out. In the same manner, there is a slight variability in ionic force between experiments, in the range 1.4–1.8 M. No clear trend emerges between the value of $\mathcal{G}_0$ and the ionic strength, due also to the quite low range of ionic strength variability. To conclude, in the present set of experiments, for an almost constant ionic strength, the effect of pH on subcritical crack growth is negligible in the range 5.5–7.5. When comparing with previous experiments using the same experimental approach [*Røyne et al.*, 2011; *Rostom et al.*, 2013], all energy release rate data fall in the range 0.2–0.4 J/m^2 (Figure 11).

3.3. Effect of Ion Species and Salinity

A combined average curve for each salt solution and concentration was determined based on the results from the individual experiments. This was done by resampling each curve, to ensure that all curves had the same number of data points. From this the average curve could be found simply by calculating the means for each point. The resulting curves can be seen in Figures 7 and 8. The calculated velocities and values for $\mathcal{G}_0$ are summarized in Table 3.

The results for NaCl are somewhat different from the results obtained by *Rostom et al.* [2013], who found $\mathcal{G}_0 = 0.40$ J/m^2 for 1 M solution of NaCl, while we have $\mathcal{G}_0 = 0.32$ J/m^2 for 1.2 M. We also have a slightly higher value for low concentrations, as *Rostom et al.* [2013] found $\mathcal{G}_0 = 0.23$–0.24 J/m^2 for 0.01 M solution of NaCl, while we have 0.28 J/m^2 for 0.012 M. However, we only ran one experiment for each concentration of NaCl. Given the high level of uncertainty in these experiments, we cannot expect to obtain exactly the same results with only one data point for each ionic solution.

MgSO$_4$ showed a similar trend as NaCl, with slightly higher values of $\mathcal{G}_0$ for high concentration than for low. The energy release rate for low concentration had an average value of 0.30 J/m^2, while for high concentration $\mathcal{G}_0$ is 0.34 J/m^2 on average. Based on the averages alone, it might appear as though a high concentration of MgSO$_4$ would cause less weakening or even a slight strengthening compared to a low concentration. However, due to the large variability between experiments with similar conditions, we cannot rule out the possibility of MgSO$_4$ having no real effect in this case.
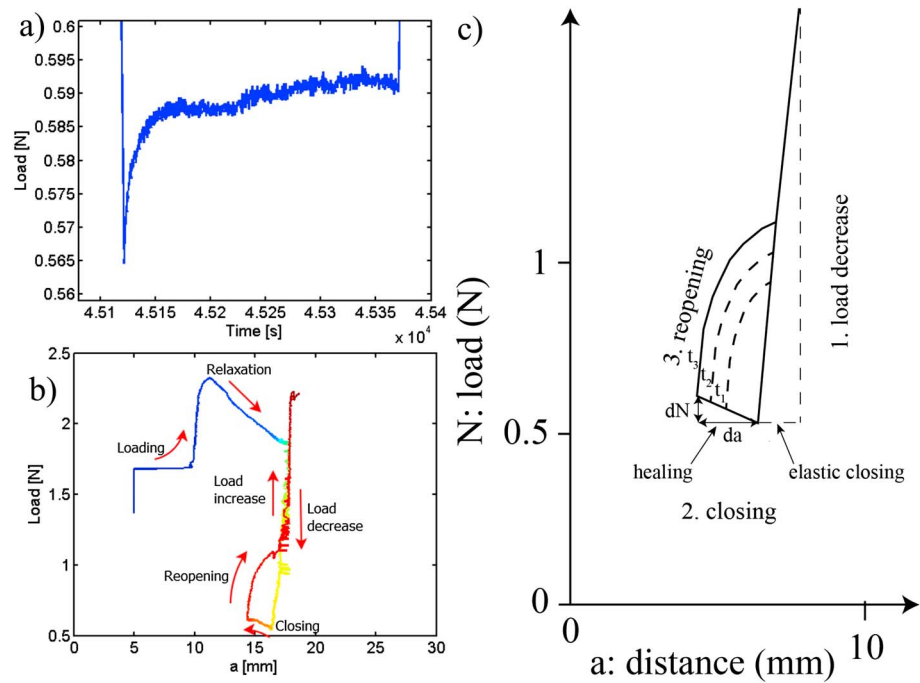
Figure 12. (a) Load curve during lightening of the load and the following relaxation for sample 140725. (b) Crack length versus load during closing of the crack for sample 141017. The color indicates time, $t = 0$ is blue. (c) Schematic representation of crack length versus load.

For $MgCl_2$ we see no significant difference in the results from high and low concentrations. For low concentrations $\mathcal{G}_0$ is 0.31 J/m^2, while at high concentration we find that $\mathcal{G}_0$ is 0.32 J/m^2. Given both a very small difference between the average values as well as a large variability for high and low concentration, $MgCl_2$ has no measurable effect on the surface energy of calcite under these specific conditions.

Na_2SO_4 stands out from the other salts. Not only is there a much more pronounced difference between high and low concentrations but we also observe a reversed effect compared to what *Rostom et al.* [2013] found for NaCl. For low concentrations $\mathcal{G}_0$ has an average value of 0.36 J/m^2. For high concentrations $\mathcal{G}_0$ is 0.27 J/m^2. Even though there is a significant variation between different experiments with the same ionic solution and concentration (see Tables 2 and 3), the two intervals do not even overlap. We conclude that we can rule out the null hypothesis and that $\mathcal{G}_0$ varies with Na_2SO_4 concentration.

3.4. Comparison to an Analytic Model

When subtracting the lower limit for the energy release rate, i.e., $\mathcal{G}_0$, in each $\mathcal{G}$ versus v curve, all the curves appear to coincide for all experiments (see insets in Figures 6–8). The theoretical expression for the $\mathcal{G}$ versus v curve is given by equation (1). There are certain discrepancies between the theoretical curve and the measured curves, most likely caused by imperfect positioning of the sample relative to the actuator.

It has been reported that there is a plateau in the $\mathcal{G}$ versus v curve (see Figure 1, region 2), until a certain value for $\mathcal{G}$, where dynamic fracture begins [*Atkinson*, 1984; *Dunning et al.*, 1994]. In previous studies on calcite single crystals, this has not been seen [*Røyne et al.*, 2011; *Rostom et al.*, 2013]. However, when we compare our data to the model fit, we see a deviation from the model for higher values of $\mathcal{G}$ ($\mathcal{G} - \mathcal{G}_0 > 0.15$ J/m^2), where the curves appear to flatten out. This may be indicative of such a plateau. However, further tests with higher loads and velocities would need to be conducted to verify this.

3.5. Crack Healing

We only have crack closing data for Na_2SO_4, $MgCl_2$, and $MgSO_4$, as the other healing results were compromised by experimental failure. In the experiments there is a difference between the optical appearance of crack length reduction and physical healing. When the aperture of the crack reduces to much less than the
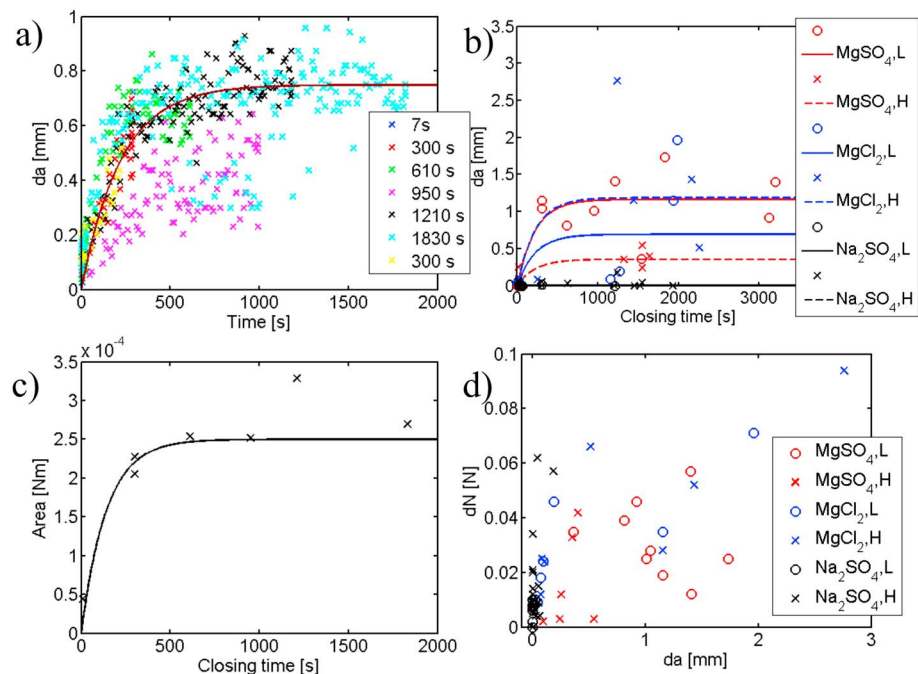
Figure 13. The extent of closing observed for different salts and concentrations. (a) The time evolution of crack closing, da, i.e., change in crack length. The different colors represent different closing intervals, occurring in series. The data is from sample 150511. The fitted line is given by da = 0.75 (mm)(1 − exp(−closing time/222(s))). (b) da is plotted against the closing interval, i.e., for how long the crack was left to close. The closing is given as an absolute difference from when the actuator was stopped until load was added again, and the crack was reopened. (c) The area mapped out by the a versus load curve (see Figure 12b) for seven different healing intervals. The fitted line is given by area = 0.25e − 3 (Nm)(1 − exp(−closing time/140(s))). All data points are from sample 150511. (d) da versus dN during closing.

wavelength of light, it cannot be detected with regular optical imaging. However, the lattice bonds will not be able to reform unless the aperture reduces further, to a few nanometers or less. Thus, the real test of whether a crack has healed, or merely narrowed, will be how the sample reacts when the crack opens up again.

Reducing the load to about 0.59 N did result in an apparent closing of the crack. In all cases a reduction in crack length was observed immediately after reducing the load, which corresponds to an elastic relaxation. However, in several cases we also saw that once the actuator had been stopped, the crack continued to shorten. In addition, the measured load increased, with an initial rapid increase lasting ∼10–30 s followed by slow creeping toward higher values, an example of which is shown in Figure 12a. This effect was not seen in every experiment, but where it was seen, it started within the first few seconds of relaxation. However, when conducting a control experiment using a steel sample, we also measured an increase in load, of the same order of magnitude as the load increase measured using calcite samples. Therefore, we cannot rule out that the measured increase in load seen in our calcite experiments is simply due to relaxation of the double torsion rig.

Crack length is plotted against load in Figure 12b. The evolution in time is indicated by a color code. The data starts out as blue (loading and relaxation), evolves to green (load decrease), then yellow (closing), and at the end red (reopening and load increase), thus showing which part of the curve is the reduction of load and which is the increase of the load again.

In the cases where the crack continued to close while the actuator was kept at a fixed position, the crack length was found to increase with load during reloading, with the same slope as during load reduction, until a threshold load was reached at which point the crack propagated back to its original position (see Figure 12b).

When the actuator is not moving, the reduction in crack length, da, appears to follow an exponential evolution in time (see Figure 13a), with a rapid initial increase before approaching an asymptote, i.e., d$a \sim a_{max}(1 - e^{-t/\tau})$, where τ represents a characteristic time scale for the crack length reduction. This suggests that some rate limiting factor slows down the crack closing as the crack aperture decreases. A similar trend is seen when comparing the total reduction in crack length with the closing interval for all experiments, shown in Figure 13b.

However, there appears to be a difference between the various salts. When comparing the amount of reduction in crack length, we see a clear trend. For Na_2SO_4 there are very few signs of any significant closing of the crack during relaxation, but for both $MgCl_2$ and $MgSO_4$ there is a clear trend of rapid closing immediately after load decrease, followed by a slower continued closing of the crack during relaxation, indicating that Mg may affect the healing of the fracture. We see no clear relation between healing and salt concentration.

The area of the hysteresis loop in the crack length versus load curve (see Figure 12b) also shows an exponential dependence on the closing interval, shown in Figure 13c. This area can be interpreted as a measure of the energy that is dissipating during the healing and reopening of the cracks. When the crack heals at a constant applied force, the surface energy is reduced, and this energy must ultimately be dissipated as heat. The hysteresis loop area is therefore a measure of the change in surface energy during crack healing. The hysteresis loop area has a similar time dependence as the crack closing, but with a τ parameter which is a little less than half the value of the fitting parameter for the curve given for the time evolution of a.

The number of previous closing intervals does not appear to affect the results significantly. We see no apparent change in crack length reduction. The area mapped out by the a versus load curve does not appear to change significantly either (see Figure 13c).

There does not appear to be any clear relation between change in load during healing, dN, and change in crack length, da, as is shown in Figure 13d. This is consistent with the assumption that the increase in load measured during healing is caused by a relaxation of the double torsion rig and is therefore most likely not related to healing.

3.6. Crack Surface Topographies
All the crack surfaces from experiments listed in Table 2 were scanned with a white light interferometer, and the areas around which the closing of the crack took place was analyzed in detail. However, there was nothing in these areas that set them apart from the rest of the crack surface.

When imaging these same areas using a scanning electron microscope, no significant differences were seen between the different sections of the same sample nor between different samples.

Four separate samples were prepared in order to investigate potential mineral deposition on the fracture surfaces. The samples were cracked in solutions of high and low concentrations of Na_2SO_4 and $MgSO_4$ and left in the solutions for ~90 min. Energy dispersive spectroscopy only showed calcium carbonate for both high and low concentrations of Na_2SO_4, as well as for low concentration of $MgSO_4$. For the sample submerged in high concentration $MgSO_4$ solution, some magnesium and sulfur was detected at the surface.

4. Discussion

Unlike most silica-rich materials which have a surface potential determined by the activity of H^+ and OH^- near $Si-O$ bonds, the potential determining ions for calcite are CO_3^{2-} and Ca^{2+} [*Stipp*, 1999]. However, adsorption of water onto the surfaces is energetically favored and has a stabilizing and relaxing effect [*de Leeuw and Parker*, 1997], which is suggested as a cause of water weakening in chalk. It has also been shown that water causes repulsion between calcite surfaces on a nanoscale [*Røyne et al.*, 2015]. Water adsorption onto the surface occurs almost immediately after surface creation, allowing for dissolution and reprecipitation within this layer [*Stipp et al.*, 1996]. Adsorption of $MgSO_4$ has also been found to reduce the surface energy of calcite [*Sakuma et al.*, 2014].

Our data show that altering the chemical composition of the fluid in contact with the sample may affect the mechanical properties of single calcite crystals, as predicted by the Rehbinder effect [*Shchukin et al.*, 2006]. Changing the surrounding fluid of the sample will affect the surface energy, thus changing the strength of the sample. Our results indicate that changing the pH has a very small effect, if any, at room temperature. Changing the salinity of either NaCl [*Rostom et al.*, 2013] or Na_2SO_4 has a somewhat greater effect, though much less than the effect of altering the water activity [*Røyne et al.*, 2011]. Magnesium salts have only a very minor effect if any at all on the surface energy of calcite at room temperature.

4.1. The Role of Calcite Dissolution
It has previously been suggested by *Atkinson* [1984] that dissolution can affect subcritical crack propagation in two ways. On the one hand, the increased solid chemical potential at the crack tip due to elastic stress concentration may lead to enhanced crack tip dissolution and drive crack propagation. This was proposed as a

mechanism for subcritical crack growth in calcite by *Atkinson* [1984]. On the other hand, dissolution at the crack tip may lead to crack tip blunting and strengthening of the crack. *Rostom et al.* [2013] suggested that tip blunting due to dissolution could explain the strengthening effect on calcite crack observed with NH_4Cl and high ionic strength NaCl saline solutions. *Dunning et al.* [1994] also proposed that dissolution could have a strengthening effect on crack propagation in calcite at low velocities. Calcite dissolution occurs by removing successive layers of calcium and carbonate ions through the nucleation and spreading of etch pits and the dissolution of preexisting steps at the mineral surface, whereas dislocation-induced dissolution is considered as a secondary effect [*Ruiz-Agudo and Putnis*, 2012]. The rate of calcite dissolution or precipitation depends on fluid chemistry. Using bulk solution experiments or atomic scale imaging, this rate is shown to be independent of pH in the range 5–8 and then it increases at lower pH [*Arvidson et al.*, 2003, Figure 1]. Atomic scale imaging have shown etch pit velocity retreat rates in the range 1.5 to 3 nm/s, depending on the steps considered *Ruiz-Agudo and Putnis* [2012]. The overall dissolution rate perpendicular to a calcite cleavage surface was measured close to 3×10^{-12} m/s at room temperature [*Arvidson et al.*, 2003]. When considering ionic strength there is a fairly large effect, and depending on the ions added to solution, these rates either decrease or increase up to 1×10^{-11} m/s for an ionic strength up to 6 M [*Ruiz-Agudo et al.*, 2009, 2010]. Nevertheless, all these dissolution rates are clearly much smaller than the smallest crack propagation velocity of 10^{-9} m/s measured during our experiments. We therefore rule out dissolution as a controlling factor in the subcritical crack propagation observed in our experiments.

4.2. Effect of pH, Ionic Strength, and Ion Species

We found that the resistance to crack propagation was not significantly influenced by pH within the range of 5–7.5 (see Figure 10). It was previously shown by *Dunning et al.* [1994] that changes in the pH of basic aqueous solutions can produce substantial shifts in crack velocity-$\mathcal{G}$ curves for calcitic rocks. However, all the solutions used in those studies were far from equilibrium with respect to calcite, which should not be the case in natural environments where the fluids are rapidly buffered when in contact with calcite. It is worth noting that the pH of the confined fluid at the fracture tip is not necessarily equal to the bulk pH at all times, as the newly formed crack will have much more reactive surfaces compared to the rest of the crystal. However, the diffusion of ions in the solution is much faster than the crack growth, and therefore any minor pH perturbations will dissipate on a much shorter time scale than the timescale of fracture growth.

Rostom et al. [2013] showed that the fracture strength of calcite increased with ionic strength for NaCl solutions ranging from 0.01 to 1 M, with a maximum value of $\mathcal{G}_0 = 0.40$ J/m^2. For ionic strengths larger than 1 M, the resistance of calcite is lower, from 0.39 to 0.26 J/m^2. In our experiments we find that $\mathcal{G}_0$ varies between 0.26 and 0.36 J/m^2 for acetic acid saturated with $CaCO_3$. When the solution is saturated, at pH 7.5 with an ionic strength equal to 3.8 M, $\mathcal{G}_0$ becomes lower than for solutions at pH 7 and varies between 0.26 and 0.3 J/m^2, which might suggest that increasing the ionic strength will increase the strength of calcite. However, our results pertaining to Na_2SO_4 do not match that assumption. As it has a noticeable strengthening effect only at low concentrations, it appears as though the nature of calcite surface energy is more complex in this respect than previously assumed. Merely increasing the ionic strength will not cause a strengthening of calcite in all cases and is clearly dependent on ion species. However, the effect of ionic strength and different ion species is less than the effect of changing the water activity by mixing in glycol [*Røyne et al.*, 2011].

Megawati et al. [2012] suggest a model for the weakening seen in chalk caused by different types of brine. This model is based on DLVO theory (named after *Derjaguin and Landau* [1941] and *Verwey and Overbeek* [1948]), and its purpose is to explain how an increased concentration in Na_2SO_4 (from 0 M to 0.22 M) causes a reduction in yield strength and bulk modulus, compared to similar tests done using NaCl (concentration ranging from 0 M to 0.63 M), which only caused a mild weakening. Their model suggests that the reduction in strength is caused by sulfate adsorption on grains near grain contacts, giving rise to a negative surface charge of the individual calcite grains. Where the grains are close, the diffusive layers overlap, causing a repulsive force between grains. However, this model would indicate that the extent of the weakening is decided by the valence and concentration of the ions injected.

If DLVO theory was sufficient to explain the results of the present study, then ion concentration and valence should be the main controlling parameter explaining the results. However, our results for different salts suggest that DLVO theory cannot give a complete description of the changes in surface energy measured in the present data set.

Heggheim et al. [2005] reported that when the concentration of NaCl was reduced from ∼0.4 M to ∼0.23 M, and the concentration of Na_2SO_4 was increased from ∼0.024 M to ∼0.096 M in their synthetic seawater, they saw an increased weakening of the chalk. This synthetic seawater also contained other salts, like $MgCl_2$ and $CaCl_2$, but the concentration of these was kept constant. Their results are consistent with our own results as well as with the results of *Rostom et al.* [2013], indicating that at least a portion of the weakening seen in chalk due to the change in concentration of these salts is due to a general reduction in the surface energy of the calcite in the grain boundaries. However, as *Heggheim et al.* [2005] varied both salt concentrations at the same time, it is difficult to determine if the change in strength is due to changing the concentration of NaCl, Na_2SO_4, or both, and in the latter case, how much is caused by which salt.

4.3. Closing and Healing of Cracks

Healing appears to occur quite rapidly in the first few seconds of crack closing and then proceeds fairly slowly afterward. This dependence on time in terms of healing is supported by the results of *Stavrinidis and Holloway* [1983], who found that leaving samples of soda-lime-glass to heal for a month caused the samples to be much stronger, i.e., greater force was necessary to reopen the crack, than samples that were left for shorter time periods. Similarly, they also found that healing was more efficient at 200°C. *Michalske and Fuller* [1985] suggested that healing in silicate glass was caused by three mechanisms, namely, first by hydrogen bonding through bridged water molecules, which in turn could bring the surfaces closer together allowing for cationic bridging and finally siloxane bridging which would completely close the gap between the two crack surfaces. However, for siloxane bridges to form any excess water left within the crack would have to diffuse into the surrounding fluid or be removed in some other fashion. Both time and increased temperature could potentially provide the mechanism for water to diffuse and allow for complete healing of the crack. Expulsion of water within the crack will thus be a rate limiting factor in the healing process, which is consistent with our measurements. The fluid within the crack must be expelled for the crack to close. Initially, this will be quite rapid, but as the two crack surfaces approach each other, the water will take on a layered structure, and expulsion requires much more energy [*Israelachvili*, 2011].

The crack closing behavior appears to have two very different contributions. Initially, the elastic closing is represented by the linear decrease in crack length with load. This is then followed by a period of irreversible closing, i.e., healing (see Figure 12c), which is partially dependent on time and chemistry. The mechanisms involved in the healing of the cracks are clearly different from those involved in the opening of the crack, as there is no correlation between which salts cause weakening and which cause a healing effect. It seems clear from our results that both magnesium salts facilitate a certain healing of the fracture while Na_2SO_4 has a much less pronounced effect. *Brantut* [2015] conducted a study on the recovery of microcrack damage in both dry and water saturated limestones. The recovery, i.e., closing or healing of microcracks, was measured in terms of permeability reduction and increase in *P* wave speed. The development in crack closing over time shows a similar trend as our results, with an initial rapid increase in *P* wave speed, followed by a gradually slower increase over time. The change in *P* wave speed is partly attributed to mechanical effects, i.e., closing of the crack, without healing or sealing taking place. However, a significant increase in recovery rate is seen in the water saturated samples compared to the dry samples, which is interpreted as an indication that microcrack closure in limestones is partly caused by pressure solution inside the cracks. Our results are also noticeably dependent on the chemistry of the system; hence, we believe that the healing we see is caused by a chemical effect, rather than a mechanical one. However, the exact mechanism or mechanisms responsible have yet to be identified.

The observation that healing in the presence of Na_2SO_4 is much lower than in the presence of $MgSO_4$ could be explained by a mechanism of passivation of the calcite surface due to precipitation of gypsum. When SO_4^{-2} ions are present at the calcite-water interface, they could bind to the calcium ions released by dissolution of calcite, forming gypsum or anhydrite. These minerals would cover the surface of the calcite, passivating it and reducing its ability to heal. In the presence of magnesium ions, this reaction is much slower because the presence of magnesium lowers the dissolution rate of calcite. Such an effect of coupled dissolution-precipitation on calcite surfaces in the presence of sulfate ions has been observed in atomic force microscope experiments *Offeddu et al.* [2014] and provides an interpretation of the difference of healing rates between these two salts. However, we see no signs of sulfate precipitation at the crack surfaces in the SEM.

4.4. Application to the Geological Sequestration of CO_2 in Carbonate Reservoirs

When supercritical CO_2 is injected into a geological formation, the pH of the pore fluid will drop as a result of the CO_2 reacting with the pore fluid to form carbonic acid. *Duan and Li* [2008] found in their numerical study of calcite dissolution that at pressures and temperatures typical of a CO_2 storage reservoir, a CO_2-saturated aqueous solution can have a significantly lower pH than 5, even if the solution is saturated with $CaCO_3$. Therefore, our results are not applicable to areas of a reservoir situated near the injection well, where the pH will drop below 5. However, further from the injection site, the pH is more likely within the range of 5 – 7.5. Based on our experimental results, it therefore appears as though injection of CO_2 into a carbonate reservoir will only have a minor effect on the mechanical strength of the host rock. Dissolution is so slow that it has very little effect on fracture growth, and increasing the concentration of $CaCO_3$ in the pore fluid will simply increase the pH again. This, in turn, is likely to slow down dissolution and eventually the system will reach a new steady state. A similar conclusion was reached by *Grgic* [2011], who found that injection of CO_2 (both supercritical and in an aqueous solution) into Lavoux limestone caused only negligible dissolution and deformation as long as the system was closed, i.e., no renewal of pore water by adding of groundwater.

When CO_2 reacts with the pore fluid, the salinity of the formation water is likely to increase, as pore water is lost by dissolving into the injected supercritical CO_2. Provided that there is significantly more NaCl than Na_2SO_4 in the pore fluid, this in turn will have a strengthening effect on the limestone, reducing subcritical fracture growth.

However, the combined effect of CO_2 injection caused by a difference in temperature between the injected CO_2 and the host rock, or the two phase effects near the injection well, are beyond the scope of this study.

5. Conclusion

We have used double torsion experiments to investigate the effect of fluid composition, salinity, and pH on subcritical fracture growth in calcite single crystals, as well as the potential for healing of cracks. Our main results are the following:

1. As long as the fluid is saturated with respect to $CaCO_3$, pH in the range 5 – 7.5 does not have a very strong effect on the surface energy of calcite. Our experimental data indicates a mild positive trend, with slightly increased strength with decreasing pH, but due to significant variability in the data, we cannot rule out the null hypothesis either.
2. At low concentrations (0.004 M) Na_2SO_4 appears to strengthen calcite crystals compared to pure water. However, at higher concentrations (0.4 M) the effect is reversed, and Na_2SO_4 seems to cause a weakening of the calcite crystal. This behavior is opposite of what has been seen for NaCl previously, suggesting that ionic strength is not sufficient to explain the effect of different salts on calcite strength.
3. $MgCl_2$ and $MgSO_4$ do not appear to have any significant effect on calcite strength, though we cannot rule out altogether that these salts have some effect on subcritical fracturing in calcite. However, both salts seem to induce healing of cracks. The underlying mechanisms that control healing are not well understood at this point and require further study.

References

Anders, M. H., S. E. Laubach, and C. H. Scholz (2014), Microfractures: A review, *J. Struct. Geol.*, *69*, 377–394.

Arvidson, R. S., I. E. Ertan, J. E. Amonette, and A. Luttge (2003), Variation in calcite dissolution rates: A fundamental problem?, *Geochim. Cosmochim. Acta*, *67*(9), 1623–1634.

Atkinson, B. K., and P. G. Meredith (1981), Stress corrosion cracking of quartz: A note on the influence of chemical environment, *Tectonophysics*, *77*(1), T1–T11.

Atkinson, B. K. (1984), Subcritical crack growth in geological materials, *J. Geophys. Res.*, *89*(B6), 4077–4114.

Baud, P., S. Vinciguerra, C. David, A. Cavallo, E. Walker, and T. Reuschlé (2009), Compaction and failure in high porosity carbonates: Mechanical data and microstructural observations, *Pure Appl. Geophys.*, *166*, 869–898.

Brantley, S. L., B. Evans, S. H. Hickman, and D. A. Crerar (1990), Healing of microcracks in quartz: Implications for fluid flow, *Geology*, *18*, 136–139.

Brantut, N. (2015), Time-dependent recovery of microcrack damage and seismic wave speeds in deformed limestone, *J. Geophys. Res. Solid Earth*, *120*, 8088–8109.

Brantut, N., M. Heap, P. Meredith, and P. Baud (2013), Time-dependent cracking and brittle creep in crustal rocks: A review, *J. Struct. Geol.*, *52*, 17–43.

Brantut, N., M. J. Heap, P. Baud, and P. G. Meredith (2014), Mechanisms of time-dependent deformation in porous limestone, *J. Geophys. Res. Solid Earth*, *119*, 5444–5463.

Brideau, M.-A., M. Yan, and D. Stead (2009), The role of tectonic damage and brittle rock fracture in the development of large rock slope failures, *Geomorphology*, *103*(1), 30–49.

Charles, R. (1958), Dynamic fatigue of glass, *J. Appl. Phys.*, *29*(12), 1657–1662.

Chen, C.-C., C.-C. Lin, L.-G. Liu, S. V. Sinogeikin, and J. D. Bass (2001), Elasticity of single-crystal calcite and rhodochrosite by Brillouin spectroscopy, *Am. Mineral.*, *86*(11–12), 1525–1529.

Croizé, D., F. Renard, K. Bjrlykke, and D. K. Dysthe (2010), Experimental calcite dissolution under stress: Evolution of grain contact microstructure during pressure solution creep, *J. Geophys. Res.*, *115*, 09207.

de Leeuw, N. H., and S. C. Parker (1997), Atomistic simulation of the effect of molecular adsorption of water on the surface structure and energies of calcite surfaces, *J. Chem. Soc. Faraday Trans.*, *93*(3), 467–475.

Derjaguin, B. V., and L. Landau (1941), Theory of the stability of strongly charged lyophobic sols and of the adhesion of strongly charged particles in solution of electrolytes, *Acta Physiochimica URSS*, *14*, 633–662.

Duan, Z., and D. Li (2008), Coupled phase and aqueous species equilibrium of the H_2O-CO_2-NaCl-$CaCO_3$ system from 0 to 250°C, 1 to 1000 bar with NaCl concentrations up to saturation of halite, *Geochim. Cosmochim. Acta*, *72*, 5128–5145.

Dunning, J., B. Douglas, M. Miller, and S. McDonald (1994), The role of the chemical environment in frictional deformation: Stress corrosion cracking and comminution, *Pure Appl. Geophys.*, *143*(1–3), 151–178.

Emberley, S., I. Hutcheon, M. Shevalier, K. Durocker, B. Mayer, W. D. Gunter, and E. H. Perkins (2005), Monitoring of fluid-rock interaction and CO_2 storage through produced fluid sampling at the Weyburn CO_2-injection enhanced oil recovery site, Saskatchewan, Canada, *Appl. Geochem.*, *20*, 1131–1157.

Evans, A. G. (1972), A method for evaluating the time-dependent failure characteristics of brittle materials—and its application to polycrystalline alumina, *J. Mater. Sci.*, *7*(10), 1137–1146.

Fan, Z., Z.-H. Jin, and S. Johnson (2012), Gas-driven subcritical crack propagation during the conversion of oil to gas, *Pet. Geosci.*, *18*(2), 191–199.

Ghassemi, A. (2012), A review of some rock mechanics issues in geothermal reservoir development, *Geotech. Geol. Eng.*, *30*(3), 647–664.

Gratier, J.-P., D. K. Dysthe, and F. Renard (2013), The role of pressure solution creep in the ductility of the Earth's upper crust, *Adv. Geophys.*, *54*, 47–179.

Gratier, J.-P., C. Noiriel, and F. Renard (2015), Experimental evidence for rock layering 709 development by pressure solution, *Geology*, *43*, 871–874.

Green, H. W. (1984), "Pressure solution" creep: Some causes and mechanisms, *J. Geophys. Res.*, *89*(B6), 4313–4318.

Grgic, D. (2011), Influence of CO_2 on the long-term chemomechanical behaviour of an oolitic limestone, *J. Geophys. Res.*, *116*, 1–22.

Griffith, A. A. (1921), The phenomena of rupture and flow in solids, *Philos. Trans. R. Soc. A*, *221*, 163–198.

Grimaldi, A., M. George, G. Pallares, C. Marliere, and M. Ciccotti (2008), The crack tip: A nanolab for studying confined liquids, *Phys. Rev. Lett.*, *100*(16), 165505.

Gutierrez, M., L. E. Øino, and K. Høeg (2000), The effect of fluid content on the mechanical behaviour of fractures in chalk, *Rock Mech. Rock Eng.*, *33*(2), 93–117.

He, S., and J. W. Morse (1993), The carbonic acid system and calcite solubility in aqueous Na-K-Ca-Mg-Cl-SO_4 solutions from 0 to 90°C, *Geochim. Cosmochim. Acta*, *57*(15), 3533–3554.

Heap, M., P. Baud, P. Meredith, S. Vinciguerra, A. Bell, and I. Main (2011), Brittle creep in basalt and its application to time-dependent volcano deformation, *Earth Planet. Sci. Lett.*, *307*(1), 71–82.

Heggheim, T., M. Madland, R. Risnes, and T. Austad (2005), A chemical induced enhanced weakening of chalk by seawater, *J. Pet. Sci. Eng.*, *46*, 171–184.

Henry, J. P., J. Paquet, and J. P. Tancrez (1977), Experimental study of crack propagation in calcite rocks, in *International Journal of Rock Mechanics and Mining Sciences and Geomechanics Abstracts*, vol. 14, pp. 85–91, Elsevier.

Israelachvili, J. N. (2011), *Intermolecular and Surface Forces*, 3rd ed., Academic Press, San Diego, Calif.

Korsnes, R. I., A. Nermoen, T. Stødle, E. Vika Storm, and M. Vadla Madland (2014), The effect of aging, temperature and brine composition on the mechanical strength of chalk, in *EGU General Assembly Conference Abstracts*, vol. 16, 14964 pp., EGU General Assembly Conference Abstracts, Vienna, Austria.

Lawn, B. (1993), *Fracture of Brittle Solids*, 2nd ed., Cambridge Univ. Press, Cambridge, U. K.

Madland, M. V., A. Hiorth, E. Omdal, M. Megawati, T. Hildebrand-Habel, R. I. Korsnes, S. Evje, and L. M. Cathles (2011), Chemical alterations induced by rock-fluid interactions when injecting brines in high porosity chalks, *Transp. Porous. Med.*, *87*, 679–702.

Main, I. G., and P. G. Meredith (1991), Stress corrosion constitutive laws as a possible mechanism of intermediate-term and short-term seismic quiescence, *Geophys. J. Int.*, *107*(2), 363–372.

Megawati, M., A. Hiorth, and M. V. Madland (2012), The impact of surface charge on the mechanical behavior of high-porosity chalk, *Rock Mech. Rock Eng.*, *46*(5), 1073–1090.

Michalske, T. A., and E. R. Fuller (1985), Closure and repropagation of healed cracks in silicate glass, *J. Am. Ceram. Soc.*, *68*(11), 586–590.

Offeddu, F. G., J. Cama, J. M. Soler, and C. V. Putnis (2014), Direct nanoscale observations of the coupled dissolution of calcite and dolomite and the precipitation of gypsum, *Beilstein J. nanotechnol.*, *5*(1), 1245–1253.

Orowan, E. (1944), The fatigue of glass under stress, *Nature*, *154*(3906), 341–343.

Parkhurst, D. L., et al. (1999), User's guide to PHREEQC (Version 2): A computer program for speciation, batch-reaction, one-dimensional transport, and inverse geochemical calculations, *U.S. Geol. Surv. Water Resour. Investigations Rep. 99-4259*, U.S. Geol. Sur., Denver, Colo.

Risnes, R., M. V. Madland, M. Hole, and N. K. Kwabiah (2005), Water weakening of chalk—mechanical effects of water-glycol mixtures, *J. Petrol. Sci. Eng.*, *48*(1–2), 21–36.

Rohmer, J., et al. (2014), Improving our knowledge on the hydro-chemo-mechanical behaviour of fault zones in the context of CO_2 geological storage, *Energy Procedia*, *63*, 3371–3378.

Rostom, F., A. Røyne, D. K. Dysthe, and F. Renard (2013), Effect of fluid salinity on subcritical crack propagation in calcite, *Tectonophysics*, *583*, 68–75.

Ruiz-Agudo, E., and C. Putnis (2012), Direct observations of mineral–fluid reactions using atomic force microscopy: The specific example of calcite, *Mineral. Mag.*, *76*(1), 227–253.

Ruiz-Agudo, E., C. Putnis, C. Jiménez-López, and C. Rodriguez-Navarro (2009), An atomic force microscopy study of calcite dissolution in saline solutions: The role of magnesium ions, *Geochim. Cosmochim. Acta*, *73*(11), 3201–3217.

Ruiz-Agudo, E., M. Kowacz, C. Putnis, and A. Putnis (2010), The role of background electrolytes on the kinetics and mechanism of calcite dissolution, *Geochim. Cosmochim. Acta*, *74*(4), 1256–1267.

Rutter, E. H. (1976), The kinetics of rock deformation by pressure solution, *Philos. Trans. R. Soc. A*, *283*, 203–219.

Røyne, A., J. Bisschop, and D. K. Dysthe (2011), Experimental investigation of surface energy and subcritical crack growth in calcite, *J. Geophys. Res.*, *116*, B04204.

Røyne, A., K. N. Dalby, and T. Hassenkam (2015), Repulsive hydration forces between calcite surfaces and their effect on the brittle strength of calcite bearing rocks, *Geophys. Res. Lett.*, *42*, 4786–4794, doi:10.1002/2015GL064365.

Sakuma, H., M. P. Andersson, K. Bechgaard, and S. L. S. Stipp (2014), Surface tension alteration on calcite, induced by ion substitution, *J Phys. Chem. C*, *118*(6), 3078–3087.

Shchukin, E., A. Bessonov, S. Kontorovich, Z. Polukarova, L. Sokolova, E. Amelina, L. Burenkova, and B. Romanovsky (2006), Effects of adsorption-active media on the mechanical propreties of catalysts and adsorbents, *Colloids Surf. A*, *282*, 287–297.

Shyam, A., and E. Lara-Curzio (2006), The double-torsion testing technique for determination of fracture toughness and slow crack growth behavior of materials: A review, *J. Mater. Sci.*, *41*(13), 4093–4104.

Stavrinidis, B., and D. G. Holloway (1983), Crack healing in glass (1983), *Phys. Chem. Glasses*, *24*(1), 19–25.

Stipp, S. L., and M. F. Hochella Jr. (1991), Structure and bonding environments at the calcite surface as observed with X-ray photoelectron spectroscopy (XPS) and low energy electron diffraction (LEED), *Geochim. Cosmochim. Acta*, *55*, 1723–1736.

Stipp, S. L. S. (1999), Toward a conceptual model of the calcite surface: Hydration, hydrolysis, and surface potential, *Geochim. Cosmochim. Acta*, *63*(19–20), 3121–3131.

Stipp, S. L. S., W. Gutmannsbauer, and T. Lehmann (1996), The dynamic nature of calcite surfaces in air, *Am. Mineral.*, *81*, 1–8.

Verwey, E. J. W., and J. T. G. Overbeek (1948), *Theory of the Stability of Lyophobic Colloids*, Elsevier, Amsterdam, Netherlands.

Wan, K.-T., and B. R. Lawn (1990), Surface forces at crack interfaces in mica in the presence of capillary condensation, *Acta Metall. Mater.*, *38*(11), 2073–2083.

Wan, K.-T., S. Lathabai, and B. R. Lawn (1990), Crack velocity functions and thresholds in brittle solids, *J. Eur. Ceram. Soc.*, *6*(4), 259–268.

Wiederhorn, S. M., and H. Johnson (1972), Effect of electrolyte pH on crack propagation in glass, *J. Am. Ceram. Soc.*, *56*, 192–197.

Zangiabadi, B., P. Kulathilagon, and B. Midtun (2011), *Evaluation of Rock-Fluid Interactions in an Outcrop Chalk: Experimental Study with MgCl$_2$ solution*, American Rock Mechanics Association, San Francisco, Calif.